Eleventh International Conference on Computational Fluid Dynamics (ICCFD11), Maui, HI, USA, July 11-15, 2022

ICCFD11-2022-xxxx

Automatic Boundary-Layer Adaptation of Structured Grids in VULCAN-CFD

A. Scholten*, P. Paredes**, F. Li***, J. White***, R. Baurle***, M. Choudhari***
Corresponding author: anton.scholten@nasa.gov

* North Carolina State University, Raleigh, NC 27695, USA.
** National Institute of Aerospace, Hampton, VA 23666, USA.
*** NASA Langley Research Center, Hampton, VA 23681, USA.

Abstract: In supersonic and hypersonic flow computations, well-resolved boundary layers are essential for accurate quantification of surface heating and transition prediction, particularly via linear stability analysis. Grid design for hypersonic flows with shocks, boundary-layer separation, and/or complex mean flow features incorporating spanwise/azimuthal inhomogeneities is a difficult issue. In comparison to a manual grid adaptation procedure, an autonomous grid adaptation technique offers significant improvements in computing time and solution quality. The VULCAN-CFD solver already includes a validated procedure for automatic adaption of structured grids to the bow shock. The present focus is on implementing an automatic boundary-layer adaptation capability in VULCAN-CFD that adapts structured, multiblock grids to both the bow shock and the boundary layer at the same time. The boundary-layer adaptation algorithm allows the user to specify the number of cells within the boundary layer, along with the input parameters used for detecting the edge of the boundary layer, namely, the variable used in the edge detection criterion, the edge detection method, the detection direction, and the relaxation factor used during the morphing of the grid. The algorithm automatically distributes grid points along the wall-normal direction to achieve a smooth variation in grid spacing from the edge of the boundary layer to a "junction" location within the outer part of the grid. Illustrative results are presented for three different high-speed configurations: a two-dimensional flow over a cylinder at Mach 17.6 and unit Reynolds number of $Re_\infty = 0.38\times10^6$ m^{-1}, an axisymmetric flow over a cone-cylinder-flare model at Mach 6.0 and $Re_\infty = 10.5\times10^6$ m^{-1}, and a three-dimensional flow over a blunt, 7-degree half-angle cone at 5-degree angle of attack in a Mach 9.79 flow with $Re_\infty = 17.1\times10^6$ m^{-1}. The automated boundary-layer adaptation is shown to provide an adequate grid topology that is aligned with the bow shock in the outer part of the grid and also resolves the viscous boundary-layer region close to the surface, thereby improving the overall quality of the solution.

Keywords: Boundary Layer Stability, Grid Adaptation.

1 Introduction

Well-resolved boundary layers are paramount to capturing the details of the boundary layer profiles for the purposes of accurate stability analysis. An automatic grid adaptation process built into Navier-Stokes flow solvers would allow a uniformly adequate boundary-layer resolution without having to invest significant effort in generating the initial grid. However, a priori design of grids to achieve such boundary-layer resolution over complex geometries is rather challenging, particularly in the presence of vortical structures that lead to significant spanwise/azimuthal variations in the boundary layer thickness. Because of this, the number of wall normal points is usually oversized, which leads to inefficient calculations.

The HIFiRE-5 flight configuration [1], consisting of a 2:1 elliptic cone, provides an excellent example of the relatively complex boundary-layer flows encountered at hypersonic speeds. It was designed to study

transition due to multiple instability mechanisms and, despite the canonical, analytical geometry, computing the laminar basic state over this model was a challenging task [2]. At a zero yaw angle, a complex vortical structure forms near the minor-axis symmetry plane, leading to strong azimuthal variation in the boundary layer thickness distribution. The challenge in designing an appropriate grid for the boundary-layer flow is compounded at nonzero yaw angles, as this vortical structure shifts away from the symmetry plane and it is no longer possible to make a priori predictions of the trajectory and the shape of this structure, as well as of the adjacent secondary structures that may form in the neighborhood of the primary structure [2]. Thus, several iterations of grid refinement and adaptation, involving both compute time and human-in-the-loop time, are required to properly resolve the boundary layer without an automated capability for boundary-layer adaptation. Another configuration that can strongly benefit from automatic boundary-layer adaption is the BOLT model [3]. Streaky structures form at several locations over the surface of the geometry, resulting in a strongly inhomogeneous boundary-layer thickness distribution [4, 5]. As a final example, the supersonic flow in the vicinity of a compression ramp includes an oblique shock upstream of the compression corner, along with an adverse pressure gradient that leads to flow deceleration, and hence, to a potential onset of flow separation, causing the boundary layer to thicken and/or lift up above the solid surface [6, 7].

Solvers such as LAURA [8] include a mature shock and boundary-layer adaptation used routinely for aerothermodynamic computations. The addition of boundary-layer adaptation in VULCAN-CFD would benefit its significant body of users as the software is commonly used for hypersonic propulsion applications and for high fidelity transition modeling based on instability analysis.

This paper provides a progress report on the implementation of automatic boundary-layer adaptation capability in the VULCAN-CFD solver [9] that enables a generic initial grid to be morphed into an improved grid that provides an appropriate resolution of the underlying flow without adding extra grid points. An outline of the paper is as follows. First, the boundary-layer adaptation algorithm is presented in Section 2. Then, the performance of this initial version of an automated boundary-layer-adaptation algorithm is illustrated in Section 3 for three canonical hypersonic flow configurations: a two-dimensional flow over a cylinder, an axisymmetric flow over a cone-cylinder-flare geometry, and a three-dimensional flow over a blunt circular cone at an angle of attack. Finally, concluding remarks and future plans are outlined in Section 4.

2 Problem Statement

Currently, the VULCAN-CFD solver has the ability to automatically adapt the grid to the shock but lacks the ability to adapt the grid to the boundary layer. As part of the present effort, an initial version of automated boundary-layer adaptation has been implemented in the VULCAN-CFD solver, with the ability to work in conjunction with the preexisting capability for shock adaptation. The adaptation follows a three step process consisting of an initial detection of the adaptation surface (shock or boundary-layer), a smoothing of the surface, and finally, the adaptation of the grid to the surface(s) of interest. The boundary-layer adaptation occurs last such that it will overwrite part of the shock-adapted grid (or unadapted grid, depending on the user's choice) extending from the surface up to an interior location that we refer to as the junction with the background grid. Detection of the boundary-layer edge is controlled by a detection quantity along with a search method and direction. The six methods available are outlined below and demonstrated on a sample function in Fig. 1. The edge can be detected as the location where the detection quantity:

1. Increases past a specified threshold (I)
2. Decreases past a specified threshold (D)
3. Reaches the global minimum (G_{min})
4. Reaches the global maximum (G_{max})
5. Reaches the first local minimum (L_{min})
6. Reaches the first local maximum (L_{max})

For each method, the search direction can be selected to start from the wall and search toward the outer boundary or in reverse. For example, the boundary-layer edge can be defined as the location where the ratio of total enthalpy to the total enthalpy in the freestream exceeds a value of 0.995. We note that there exist alternate metrics to define the boundary-layer edge and those can be easily added in the future. The provided detection capability aims to allow the user to detect the desired edge location while accounting for potentially nonmonotonic variation in the detection quantity with respect to increasing distance from the solid surface. A safety factor can also be provided and may be used as necessary to multiply the distance from the surface to the detected boundary-layer edge and redefine the boundary-layer edge at a larger (or shorter) distance.

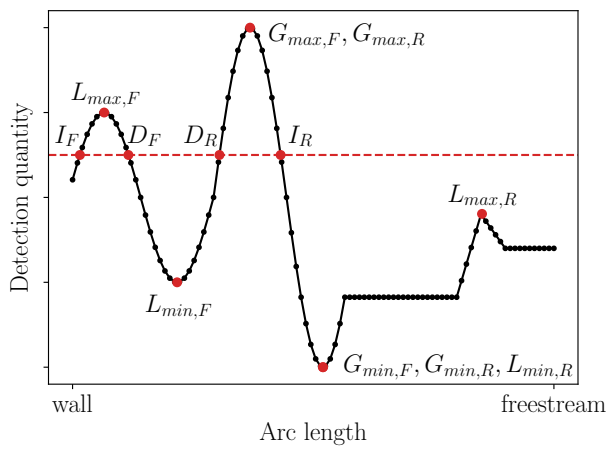

Figure 1: Resulting edge location using the six different methods in either the forward, F, or reverse, R, search direction on an arbitrary function. The red dashed line indicates the provided threshold.

In order not to disturb the current shock adaptation capability of the solver, the addition of the boundary layer adaptation has to be smoothly merged with the output grid from shock adaptation. To illustrate the adaptation process implemented, Fig. 2 provides the grid spacing and arc length for an arbitrary grid line at three key locations. The shaded regions below the grid spacing of Fig. 2(a) illustrates the integral of the grid spacing corresponding to the arc length at specific indices, shown as the colored points in Fig. 2(b). As the user provides the number of points within the boundary layer (n_{ble}) and the location of the boundary-layer edge (S_{ble}) by specifying the detection parameter, the adaptation process has to calculate a grid distribution that will satisfy these criteria while also smoothly connecting to the existing grid. To achieve this, we define the grid by using the spacing between surface-tangent grid lines, which corresponds to the spacing between points along a wall-normal grid line. Because the integral of the spacing equals the grid line's arc-length, setting the integral to a specific value will guarantee that the grid extends up to a predetermined location. This location will act as the junction location (S_{jun}) with the original grid that may be either unadapted or shock adapted. To ensure a smooth transition from the adapted boundary-layer grid with the original grid beyond the junction location, the grid spacing at the junction location must match the existing grid spacing. Thus, the boundary-layer adapted grid consists of two regions: the boundary layer region extending to the boundary-layer edge with a constant grid spacing, and a junction region extending from the boundary-layer edge to either the freestream boundary or to a location before the outer shock (if adapted).

The grid points can be distributed within the boundary-layer region with constant spacing as all required parameters are already defined once the edge is detected and number of points calculated. In contrast, defining the grid spacing for the junction region requires more attention as there are four constraints to satisfy:

1. The integral of the spacing function within the junction region has to equal the arc-length between the boundary-layer edge and the junction location.
2. The number of points within the junction region is defined by the number of points in the boundary-layer and the junction location.

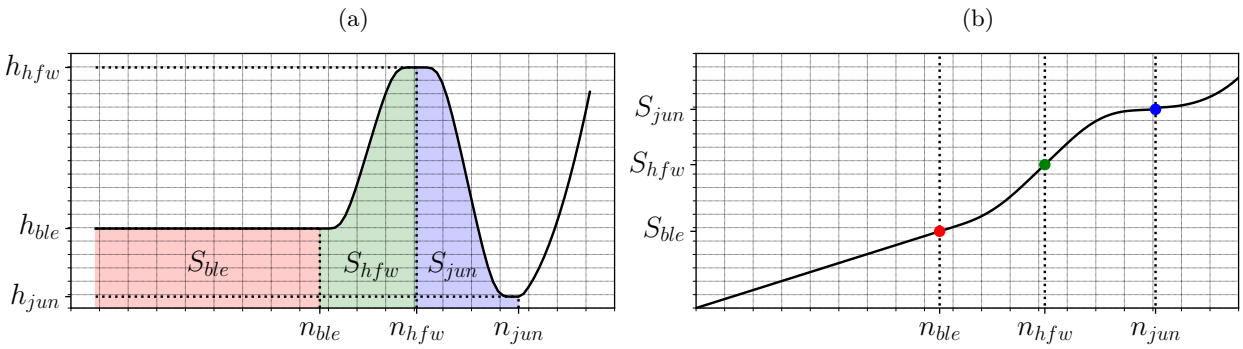

Figure 2: (a) Grid spacing and (b) arc length from the surface to any point along a sample grid line to illustrate the algorithm used. The shaded areas below the grid spacing line are equal to the arc length between the grid indices of interest: n_{ble}, n_{hfw}, and n_{jun} corresponding to the boundary-layer edge, halfway, and junction indices respectively.

3. The spacing at the boundary-layer edge has to be smoothly matched.
4. The spacing at the junction location has to be smoothly matched.

As these constraints are grid and solution dependent, certain desirable constraints cannot be imposed. For example, the spacing at the boundary-layer edge may be smaller than the spacing at the junction for some cases. However, if the grid is shock adapted and the junction is set too close to the shock, the grid spacing could be smaller there than within the boundary layer. Thus to accommodate a variety of cases, two functions are used with a shared point (i.e., equal spacing at the connection between them), selected at the index halfway between the boundary-layer edge index and the junction location index, indicated as n_{hfw} on Fig. 2. This selection allows both functions to have enough resolution for coarser grids, but does influence the spacing at this connection. Improvements currently being implemented will allow the halfway index to be changed automatically to avoid an adaptation error resulting in a negative grid spacing (which could also be resolved by altering the number of points within the boundary-layer). The first function will either increase or decrease the grid spacing while the second function will do the opposite in the boundary-layer edge to halfway location and halfway to junction locations, respectively. This allows the endpoints to have grid spacing matched with the boundary layer and the previous grid while also providing the flexibility to choose the grid spacing at the halfway location where both functions connect. The halfway location will then be used to satisfy the first constraint to make sure the grid fills the entire space between the boundary-layer edge and junction to the previous grid. The second constraint will be satisfied when numerically integrating the spacing to obtain the grid point locations. Various calculations for selected test cases demonstrated that adding the grid spacing between each grid point will leave a considerable error as compared to using a simple trapezoidal integration, reducing the error enough to not have an effect. The last two constraints are satisfied by choosing smooth functions.

As such, two smooth (C-infinity) approximations to the Heaviside step function are used in the junction region to accommodate the previously discussed constraints. Consider the function

$$f(t) = \begin{cases} -1; & t \in (-\infty, -1], \\ \tanh(1/(1-t) - 1/(1+t)); & t \in (-1, 1), \\ 1; & t \in [1, \infty). \end{cases} \tag{1}$$

It can be shown that $f(t)$ and its derivatives of all orders are continuous on the entire real axis. This C-infinity function and its derivative are shown in Fig. 3(a). The function can be translated and dilated with a general form

$$H(t;\ t_0, t_1) = \frac{1}{2}\Big(1 + f\Big(\frac{2t - (t_1 + t_0)}{t_1 - t_0}\Big)\Big), \tag{2}$$

giving us a C-infinity Heaviside function with a smooth step between t_0 and t_1 as visible on Fig. 3(b). A

crucial benefit of this function is the known value of its integral within the step

$$\int_{t_0}^{t_1} H(t;\ t_0, t_1)\ dt = \frac{t_1 - t_0}{2}. \tag{3}$$

The above equality holds when we analytically perform this integration. With a finite number of grid points, the discrete value of this integral is used to avoid discontinuities at the junction between the newly adapted and previous grids.

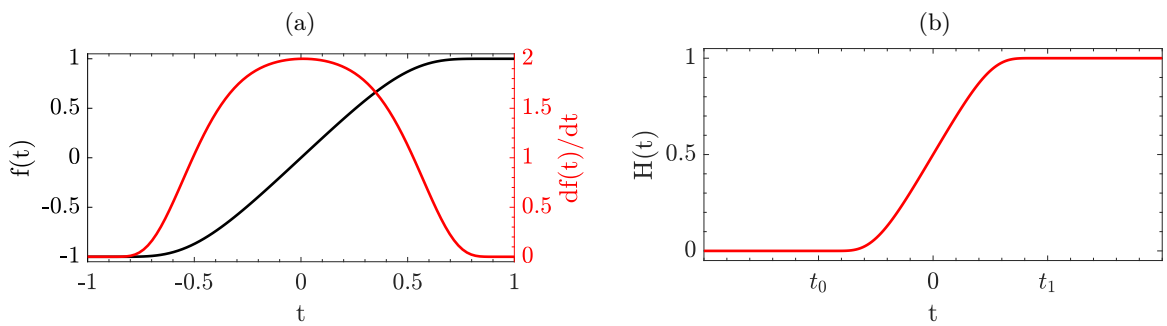

Figure 3: (a) C-infinity step function and its first derivative and (b) C-infinity Heaviside function.

After detecting the boundary-layer edge and adapting the grid to the shock, the following known parameters

- n_{ble}, S_{ble}: number of points (i.e, index) and location of the boundary-layer edge obtained from the boundary-layer-edge detection;
- n_{jun}, h_{jun}, S_{jun}: index, grid spacing, and location of the junction location obtained from the grid dimensions or calculated using the shock location;

are used to calculate the constant spacing within the boundary-layer (h_{ble}) and the index of the halfway location (n_{hfw}), connecting both C-infinity functions

- $h_{\text{ble}} = \frac{S_{\text{ble}}}{n_{\text{ble}}}$,
- $n_{\text{hfw}} = \frac{n_{\text{ble}} + n_{\text{jun}}}{2}$.

As the location between both C-infinity functions is set at the index n_{hfw} that is halfway between the boundary-layer-edge and junction indices, the last parameter needed to obtain the grid spacing for all points is the spacing h_{hfw} at the halfway index. This can be derived from the arc-length at different locations:

$$S_{\text{hfw}} = S_{\text{ble}} + h_{\text{ble}}(n_{\text{hfw}} - n_{\text{ble}}) + \frac{h_{\text{hfw}} - h_{\text{ble}}}{2}(n_{\text{hfw}} - n_{\text{ble}}), \tag{4}$$

$$S_{\text{jun}} = S_{\text{hfw}} + h_{\text{hfw}}(n_{\text{jun}} - n_{\text{hfw}}) + \frac{h_{\text{jun}} - h_{\text{hfw}}}{2}(n_{\text{jun}} - n_{\text{hfw}}), \tag{5}$$

which we can solve for h_{hfw},

$$h_{\text{hfw}} = \frac{2}{n_{\text{jun}} - n_{\text{ble}}}\Big(S_{\text{jun}} - S_{\text{ble}} - \frac{h_{\text{ble}}}{2}(n_{\text{hfw}} - n_{\text{ble}}) - \frac{h_{\text{jun}}}{2}(n_{\text{jun}} - n_{\text{hfw}})\Big). \tag{6}$$

With all parameters defined, the spacing at each grid point ($h(n)$) can be calculated as:

$$h(n) = \begin{cases} h_{\text{ble}}; & n = 1,\ n_{\text{ble}}, \\ h_{\text{ble}} + (h_{\text{hfw}} - h_{\text{ble}}) \cdot H(n;\ n_{\text{ble}}, n_{\text{hfw}}); & n = n_{\text{ble}} + 1,\ n_{\text{hfw}}, \\ h_{\text{hfw}} + (h_{\text{hfw}} - h_{\text{ble}}) \cdot H(n;\ n_{\text{hfw}}, n_{\text{jun}}); & n = n_{\text{hfw}} + 1,\ n_{\text{jun}}. \end{cases} \tag{7}$$

Finally, the location $S(n)$ for a point with index n along the grid line is given by a numerical integration:

$$S(n) = \begin{cases} 0; & n = 1, \\ S(n-1) + h(n-1); & n = 2,\ n_{\text{ble}}, \\ S(n-1) + h(n-1) + \frac{h(n)-h(n-1)}{2}; & n = n_{\text{ble}} + 1,\ n_{\text{jun}}. \end{cases} \tag{8}$$

As previously mentioned, the trapezoidal integration is used for the variable grid spacing to ensure a smooth connection to the previous grid.

3 Results

The application of the automatic boundary-layer adaptation in VULCAN-CFD solver is presented for three high-speed test cases that are listed in Table 1.

Table 1: Flow conditions used for the three test cases: a 2D cylinder, an axisymmetric cone-cylinder-flare model (CCF), and a 3D blunt cone at angle of attack.

Case	M_∞	u_∞ [m/s]	ρ_∞ [kg/m^3]	T_∞ [K]	T_0 [K]	T_{wall} [K]	P_0 [Pa]	Re_∞ [m^{-1}]
2D Cylinder	17.6	4991	0.001	200	12597.4	500	1.1423×10^8	0.3769×10^6
Axisymmetric CCF	6	862	0.043	51.4	421.5	300	1.0318×10^6	10.46×10^6
3D Blunt Cone at AoA	9.79	1401	0.044	51	1028.6	300	2.3745×10^7	17.10×10^6

3.1 Two-Dimensional Flow over a Cylinder at Mach 17.6

The two-dimensional flow over a cylinder with a 1 m radius in a Mach 17.6 free stream represents a canonical problem for viscous high-speed conditions. For the purpose of illustrating the performance of the adaptation algorithm, we use a grid that consists of 61×65 points. This configuration is run with shock adaptation alone and also with both shock and boundary-layer adaptations. Here, the boundary-layer edge is defined as the location where the ratio of total enthalpy to the total enthalpy in the freestream exceeding a value of 0.9. The Mach contours of the converged solutions are shown in Fig. 4. For this case, the original grid was already well tailored to the viscous gradient adjacent to the surface, and therefore, the boundary-layer adaptation only slightly increased the number of points inside the boundary layer. The distribution of grid points along the light blue grid line from Figs. 4(b) and 4(c) is shown in Fig. 5(b). The algorithm did not adjust any points beyond the junction location but ensured that the spacing remained continuous across the junction.

3.2 Axisymmetric Flow over a Cone-Cylinder-Flare model at Mach 6

The second geometry corresponds to an axisymmetric cone-cylinder-flare with 0.1 mm nosetip radius, 5-degree half-angle cone, 12.6 cm long cylinder, and a 10-degree half-angle flare. This geometry was used in the experiments conducted by Benitez et al. [10, 11] in the Boeing/AFOSR Mach 6 Quiet Tunnel (BAM6QT) at Purdue University and computationally investigated in Refs. [12, 13]. Again, to illustrate the performance of the grid adaptation algorithm, we use a grid of 601×301 points that is substantially coarser in comparison with the grids employed in previous studies [12, 13]. For parallel computation, the grid is split into 40 blocks along the streamwise direction to test the boundary layer adaptation capability across multiple streamwise subdomains. Solutions are obtained with shock alignment alone and with both shock and boundary-layer adaptations. Similar to the previous case, the boundary-layer edge is defined using the total enthalpy ratio exceeding a value of 0.95. While acceptable residual convergence was obtained in both computations, significant differences are observed between the corresponding predictions of boundary-layer thickness across the separation region, the length of the separation region, and the locations of the separation and reattachement shocks. Figure 6(a) shows the Mach contours for the solution with both boundary-layer and shock adaptation as well as the separation region limits for both solutions. Figures 6(b) and 6(c) show a closer view of the

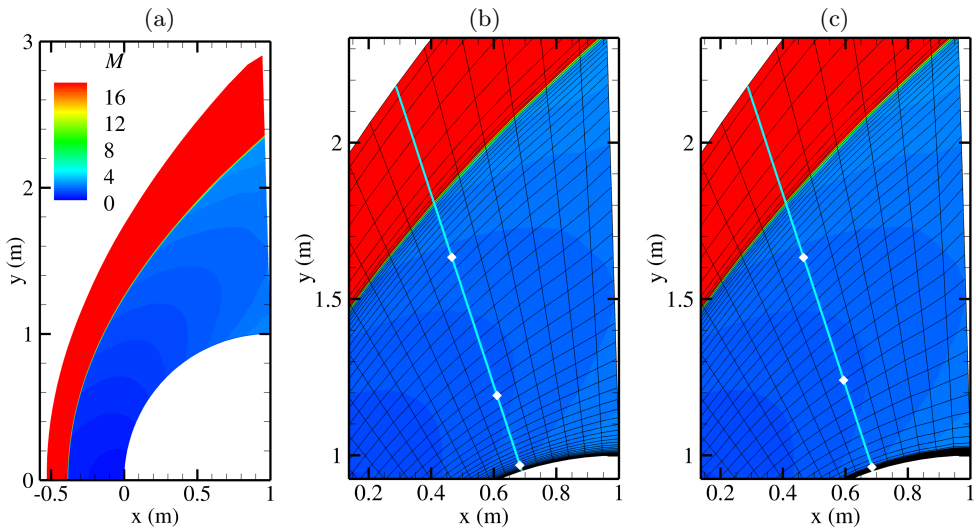

Figure 4: (a) Mach contours of the Mach 17 cylinder flow over the upper half of the computational domain for the boundary-layer and shock adapted grid. A zoomed view of the grid and Mach contours corresponding to the (b) shock-adapted and (c) both shock- and boundary-layer-adapted solutions. The grid spacing and arc length distributions along the grid line indicated by the light blue line from each of the subfigures (b) and (c) are shown in Figs. 5(a) and 5(b), respectively. The white diamonds correspond to the indices n_{ble}, n_{hfw}, and n_{jun}.

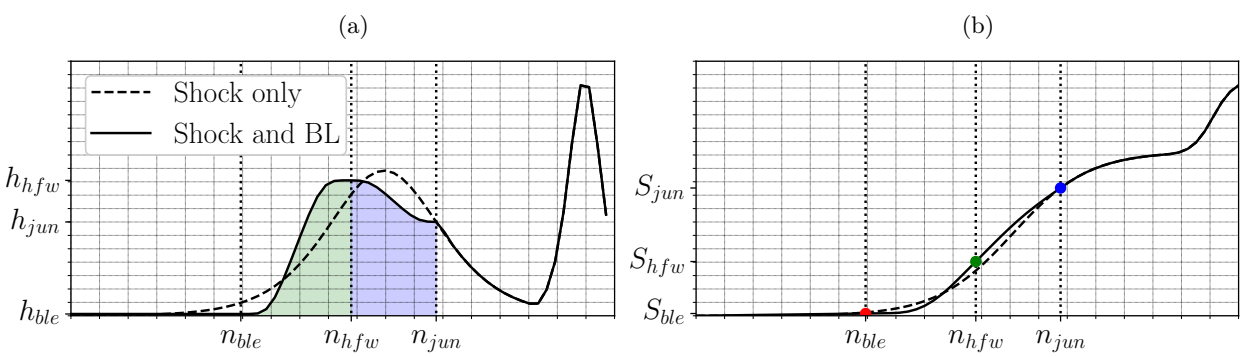

Figure 5: (a) Grid spacing and (b) arc length from the surface to any point along the light blue grid lines shown in Figs. 4(b) and 4(c). The shaded areas below the grid spacing line are equal to the arc length between the grid indices of interest (n_{ble}, n_{hfw}, and n_{jun}).

corner, with a distinct difference in grid resolution. The separation region of the shock adapted solution is poorly resolved, leading to an underprediction of its length compared to the solution using both shock and boundary-layer adaptation. The difference in resolution along the light blue grid line is visible on Fig. 7(a). The shift in maximum spacing further away from the wall, as shown by the dashed and solid black lines, illustrates the algorithm redistribution of points to satisfy the requested number within the boundary-layer without increasing the maximum grid spacing between the boundary-layer edge and the shock, nor decreasing the shock's resolution. To demonstrate the flexibility of the boundary-layer adaptation at capturing the reattachement shock, a solution was computed using the boundary-layer edge defined as the location of the Mach number to freestream Mach number exceeding a value of 0.85. The reattachement region of the enthalpy- and Mach number-based boundary-layer adaptations are shown in Figs. 8(a) and 8(b), respectively. Although the Mach number adapted grid was able to accurately align with the reattachement shock, the wall-normal grid spacing toward the end of the domain may not be fine enough to resolve the boundary layer.

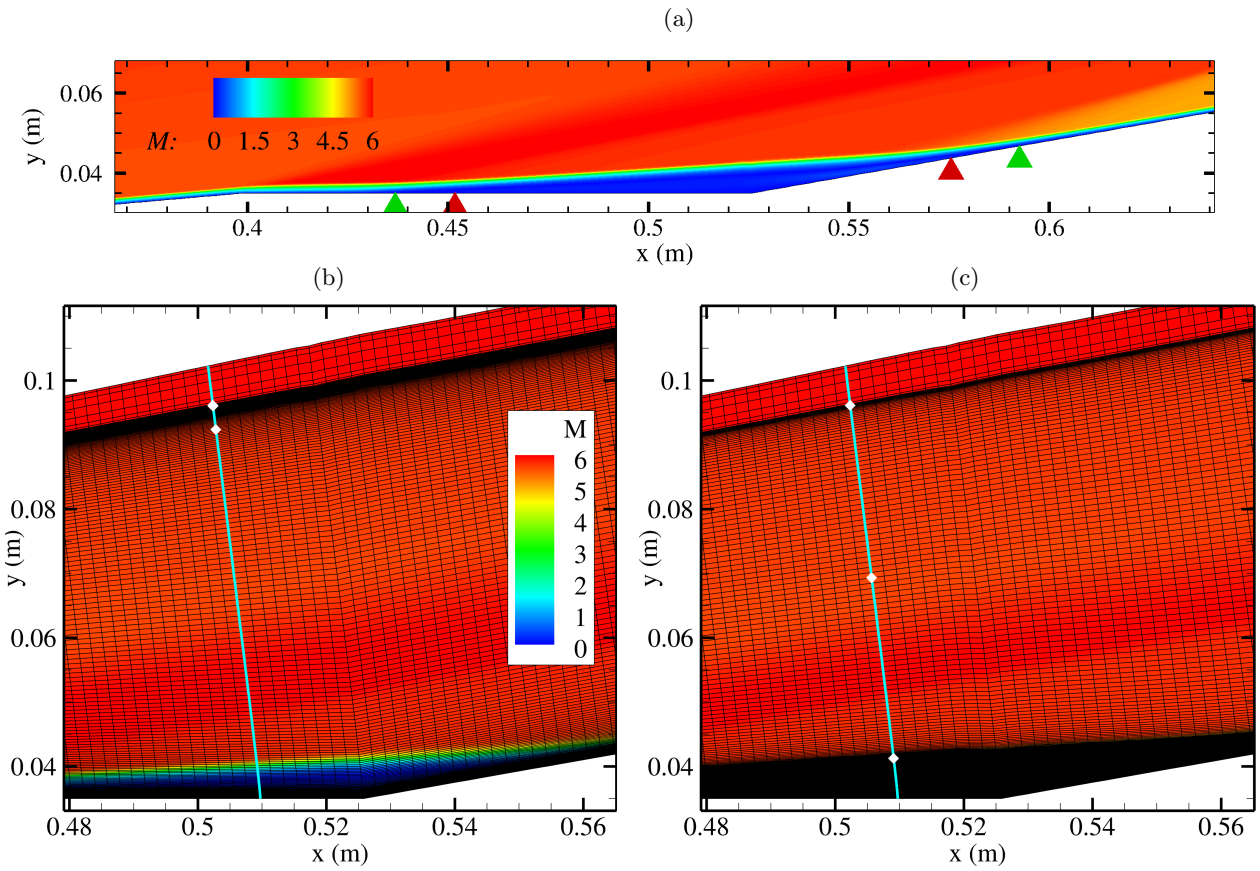

Figure 6: (a) Mach contours over the separation region of the shock and boundary-layer adapted flow over the axisymmetric cone-cylinder-flare at Mach 6. The red triangles indicate the start and end of the separation region obtained with only shock adaptation while the green ones are for the shock and boundary-layer adapted separation region. Mach contours zoomed in the corner region of the (b) shock and (c) shock and boundary-layer adapted solutions. Similar to Fig. 4, the light blue lines and white diamonds are shown in Fig. 7.

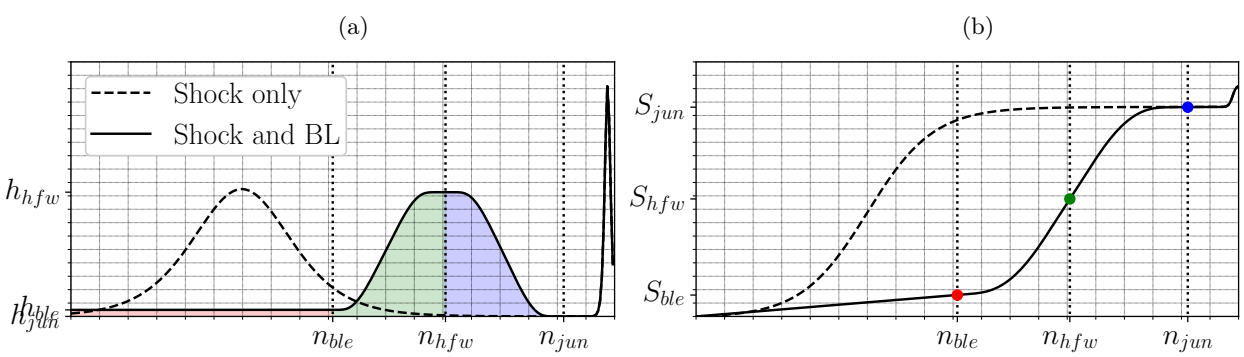

Figure 7: (a) Grid spacing and (b) arc length from the surface to any point along the light blue grid lines shown in Fig. 6(b,c). The shaded areas below the grid spacing line are equal to the arc length between the grid indices of interest (n_{ble}, n_{hfw}, and n_{jun}).

3.3 Three-Dimensional Flow over a Blunt Circular Cone at Angle of Attack

The final configuration corresponds to a 1.5 meters long, 7 degrees half-angle cone with 9.525 mm nosetip at Mach 9.79 and 5 degrees angle of attack, following the previous experiments [14, 15] and computations [16].

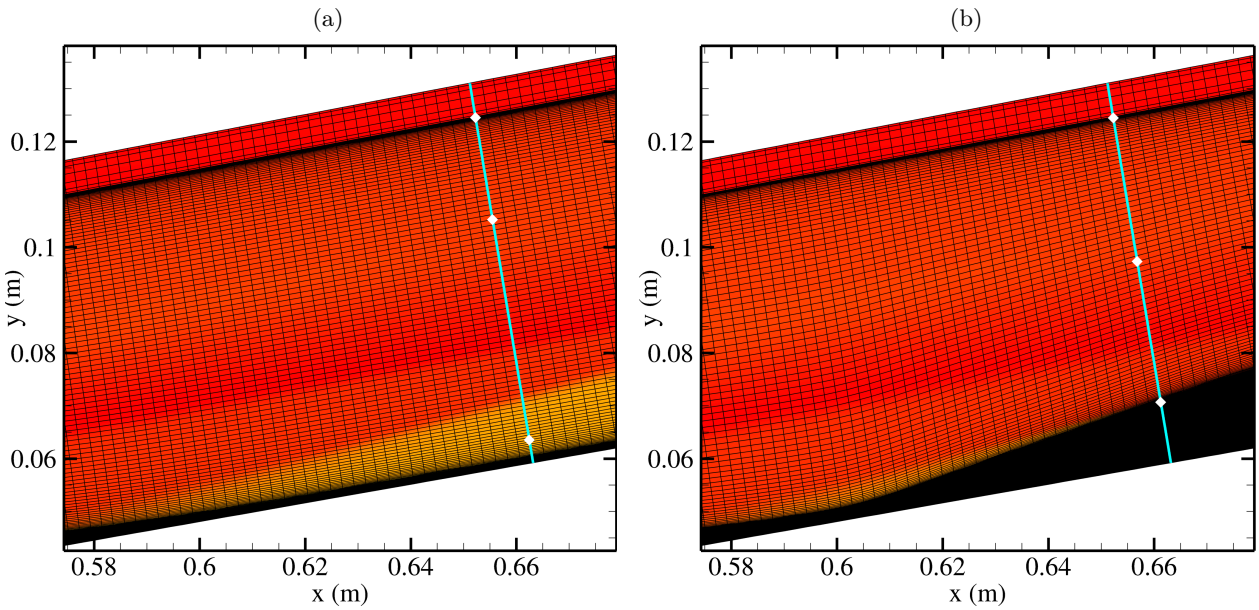

Figure 8: Mach contours of the axisymmetric cone-cylinder-flare at Mach 6 zoomed in the reattachement region of the shock and boundary-layer adapted solutions using (a) an enthalpy- and (b) a Mach number-based boundary-layer edge detection. The white diamonds along the light blue lines represent the indices n_{ble}, n_{hfw}, and n_{jun} obtained by the Mach detection method to illustrate the difference in grid distribution.

The freestream conditions listed in Table 1 are selected to replicate those of the experiments. The Keyes' law for diatomic Nitrogen [17] is used to calculate the viscosity as a function of temperature. An isothermal wall temperature of 300 K is selected. Preliminary results using a very coarse grid for this configuration are compared with those used by Ref. [16] to illustrate the ability of the algorithm to adapt the boundary layer to the leeward vortical structure. The computational grid solves half the geometry and imposes symmetry conditions along the windward and leeward planes. The grid is composed of a nosetip block and a frustum block to avoid the nosetip axis singularity, and consists of two blocks of $9 \times 17 \times 45$ and $105 \times 33 \times 45$ points. The frustum block is then split in both the surface tangent and azimuthal direction to ensure the boundary-layer adaptation will not cross a block boundary and is not affected by the subdivision of the domain. Mach contours at different streamwise slices are shown on Fig. 9 for the boundary-layer and shock adapted solution. Although not shown here, the convergence history significantly improved by adding the boundary-layer adaptation even with the very coarse grid used. Furthermore, the shape of the leeward vortex differs for both solutions as shown in Figs. 10(a) and 10(b), highlighting the solver's newly added ability in allowing coarser grids to retain resolution in the boundary layer. As observed in Fig. 11, the grid points around the shock were also altered as each of the 3 grid adaptation cycles performed by the solver affected the solution used for the next adaptation. The boundary-layer adaptation algorithm itself did not change the point distribution beyond the junction location, defined as a few points below the shock. A finer mesh, or one split in two blocks in the wall-normal direction, would have avoided this issue. The shock adapted grid kept significantly fewer points within the boundary layer, indicated by the initial increase in grid spacing of Fig. 11(a). A split of the grid in the wall-normal direction could have helped retain points within the boundary-layer for the shock-adapted grid but would have not provided the much needed, azimuthally varying, adaptation to the forming vortex.

4 Conclusion and Future Work

To allow accurate computations of boundary-layer flows over hypersonic configurations, particularly for the purpose of transition prediction based on linear stability analysis, a preliminary capability for automatic boundary-layer adaptation has been implemented in the VULCAN-CFD code and demonstrated for three

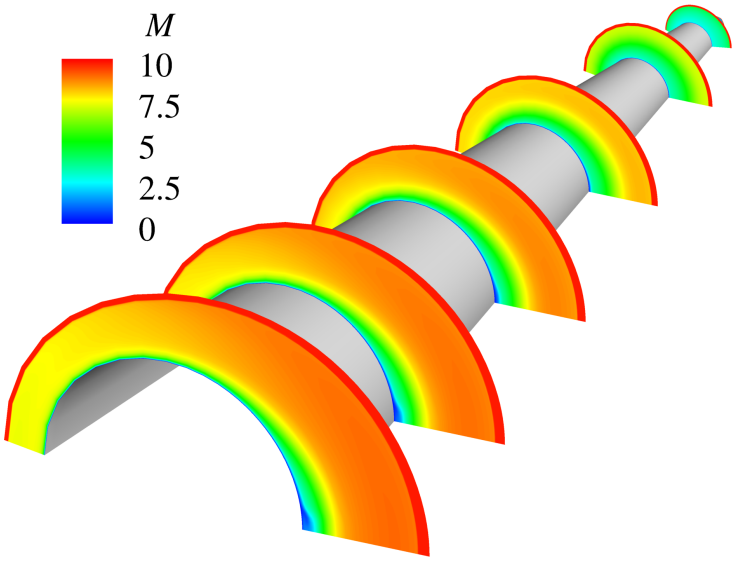

Figure 9: Mach contours on 6 arbitrary streamwise-normal slices over the boundary-layer and shock adapted solution for the 3D blunted cone at 5 degrees AoA in a Mach 9.79 freestream.

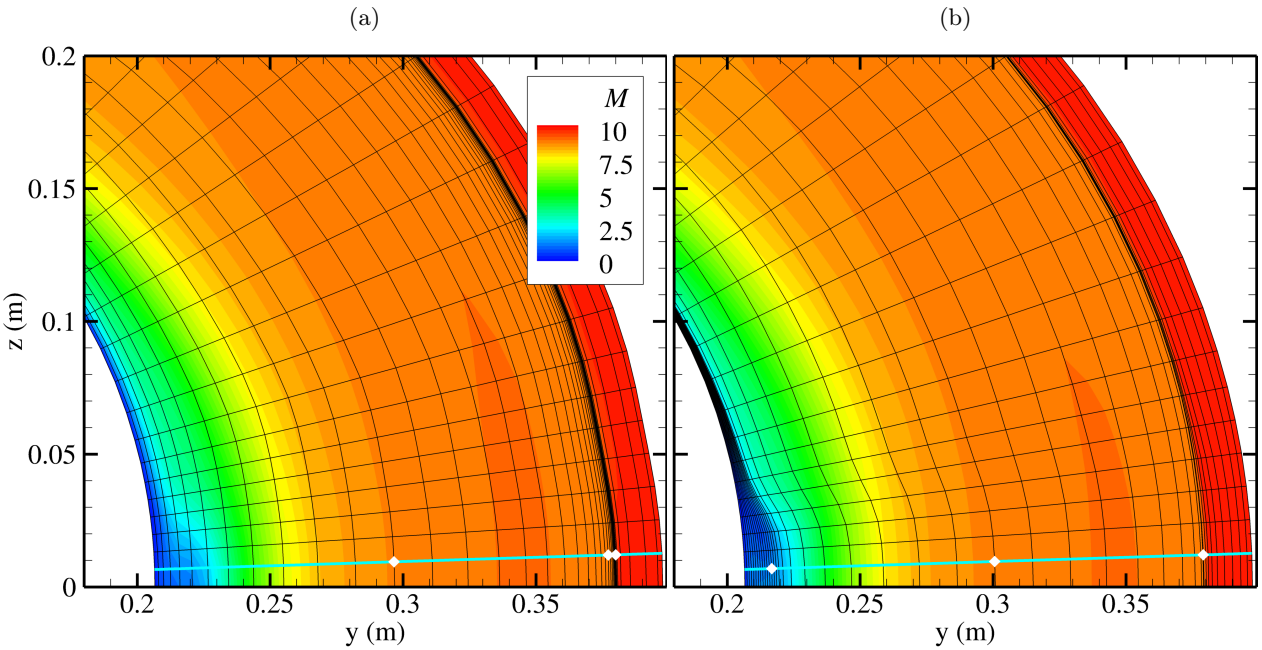

Figure 10: Mach contours of the 3D blunted cone at 5 degrees AoA in a Mach 9.79 freestream. The cross-section at $x = 1.495$ m on the leeward side is shown for the (a) shock and (b) shock and boundary-layer adapted grids. The point distributions of the light blue grid lines are shown in Fig. 11.

test cases with laminar boundary layers, namely, the two-dimensional flow over a cylinder at Mach 17.6, the axisymmetric flow over a cone-cylinder-flare at Mach 6, and the three-dimensional flow over a blunt circular cone at a nonzero angle of attack at Mach 9.79. The details of the boundary-layer adaptation algorithm are presented. The properties of the function selected to calculate the grid spacing ensures a smooth transition

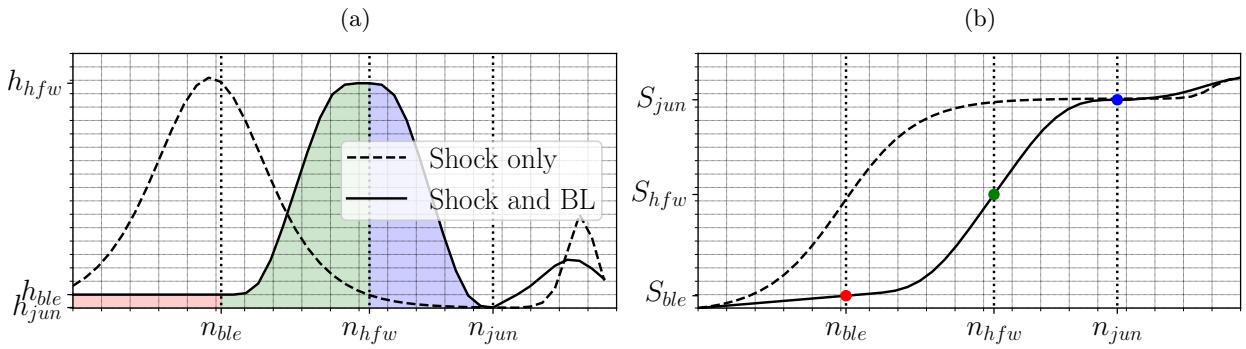

Figure 11: (a) Grid spacing and (b) arc length from the surface to any point along the light blue grid lines shown in Fig. 10(a,b). The shaded areas below the grid spacing line are equal to the arc length between the grid indices of interest (n_{ble}, n_{hfw}, and n_{jun}).

between the boundary-layer region adjacent to the surface and the outer region with either an unadapted or a shock-adapted grid. Further improvements to the adaptation process will include the evaluation and further improvement of the boundary-layer adaptation for turbulent boundary layers as well as for flows with laminar, transitional, and fully turbulent regions. Furthermore, we plan to incorporate additional criteria for detecting the edge of the boundary layer, a user-defined junction location, and the detection and adaptation of interior features, such as internal regions of high gradients associated with a separated boundary layers and/or a reattachment shock.

Acknowledgments

This material is based upon research supported by the U. S. Office of Naval Research under award number N00014-20-1-2261 and by the Hypersonic Technology Project (HTP) under the NASA Aeronautics Research Mission Directorate (ARMD). The computational resources for this work were provided by the DoD High Performance Computing Modernization Program, the NASA High-End Computing (HEC) Program through the NASA Advanced Supercomputing (NAS) Division at the Ames Research Center, and the LaRC K-Midrange Cluster at the Langley Research Center.

References

[1] R. Kimmel, D. Adamczak, K. Berger, and M. Choudhari. HIFiRE-5 flight vehicle design. AIAA Paper 2010-4985, 2010.

[2] M. Choudhari, C.-L. Chang, T. Jentink, K. Berger, G. Candler, and R. Kimmel. Transition analysis for the HIFiRE-5 vehicle. AIAA Paper 2009-4056, 2019.

[3] B. Wheaton, D. Berridge, T. Wolf, D. Araya, R. Stevens, B. McGrath, B. Kemp, and D. Adamczak. Final design of the boundary layer transition (BOLT) flight experiment. AIAA Paper 2020-1041, 2020.

[4] J. Thome, A. Knutson, and G. Candler. Boundary layer instabilities on BoLT subscale geometry. AIAA Paper 2019-0092, 2019.

[5] F. Li, M. Choudhari, and P. Paredes. Streak instability analysis for bolt configuration. AIAA Paper 2020-3028, 2020.

[6] J. Becker and P. Korycinsky. Heat transfer and pressure distribution at a Mach number of 6.7 on bodies with conical flares and extensive flow separation. Technical Report RM L56F22, NACA, 1956. DTIC citation AD0274584.

[7] D. Chapman, D. Kuehn, and H. Larson. Investigation of separated flows in supersonic and subsonic streams with emphasis of the effect of transition. Technical Report TR 1356, NACA, 1958. NTRS number 19930092343.

[8] K. Thompson, B. Hollis, C. Johnston, B. Kleb, V. Lessard, and A. Mazaheri. LAURA users manual: 5.6. Technical Report NASA/TM-2020-220566, NASA Langley Research Center, 2020.

[9] R. Baurle, J. White, T. Drozda, and A. Norris. VULCAN-CFD user manual: Ver. 7.1.0. Technical Report NASA/TM-2020-5000767, NASA Langley Research Center, 2020.

[10] E.K. Benitez, J.S. Jewell, S.P. Schneider, and S. Esquieu. Instability measurements on an axisymmetric separation bubble at Mach 6. AIAA Paper 2020-3072, 2020.

[11] E.K. Benitez, J.S. Jewell, and S.P. Schneider. Separation bubble variation due to small angles of attack for an axisymmetric model at Mach 6. AIAA Paper 2021-0245, 2021.

[12] P. Paredes, A. Scholten, M. Choudhari, F. Li, E. Benitez, and J. Jewell. Boundary-layer instabilities over a cone-cylinder-flare model at Mach 6. AIAA Paper 2022-0600, 2022.

[13] F. Li, M. Choudhari, P. Paredes, and A. Scholten. Nonlinear evolution of instabilities in a laminar separation bubble at hypersonic Mach number. AIAA Paper 2022-0000, 2022.

[14] E.C. Marineau, C.G. Moraru, D.R. Lewis, J.D. Norris, J.F. Lafferty, R.M. Wagnild, and J.S. Smith. Mach 10 boundary-layer transition experiments on sharp and blunted cones. AIAA Paper 2014-3108, 2014.

[15] C. Moraru. Hypersonic boundary-layer transition measurements at Mach 10 on a large seven-degree cone at angle of attack. Master's thesis, Purdue University, 2015.

[16] P. Paredes, A. Scholten, M. Choudhari, and F. Li. Hypersonic boundary-layer transition on blunted cones at angle of attack. AIAA Paper 2021-2886, 2021.

[17] C.J. Roy and F.G. Blottner. Review and assessment of turbulence models for hypersonic flows. *Progress in Aerospace Sciences*, 42:469–530, 2006.